

Quantitative analysis of galaxy-galaxy lensing

Peter Schneider¹ and Hans-Walter Rix^{1,2}

¹ Max-Planck-Institut für Astrophysik
Postfach 1523, D-85740 Garching, Germany

² Steward Observatory
University of Arizona, Tucson, AZ 85721, USA

Abstract

Gravitational light deflection due to mass along the line-of-sight will distort the images of background sources. This effect has been used successfully to investigate the mass distribution of galaxy clusters. Although an individual galaxy is not massive enough to cause a detectable lensing distortion in the background population, this effect can be measured statistically for a population of galaxies, and a first detection was reported recently by Brainerd, Blandford and Smail (BBS).

In this paper we explore a quantitative and efficient method to constrain the halo properties of distant galaxy populations through “galaxy-galaxy” lensing and show that the mean masses and sizes of halos can be estimated accurately, without excessive data requirements. Specifically, we propose a maximum-likelihood analysis which takes full account of the actual image ellipticities, positions and apparent magnitudes. We apply it to simulated observations, using the same model for the lensing galaxy population as in BBS, where the galaxy halos are described by isothermal spheres with velocity dispersion σ , truncated at a radius s . Both parameters are assumed to scale with the luminosity of the galaxy. The best fitting values, σ_* and s_* , corresponding to an L_* -galaxy, are then determined with the maximum-likelihood analysis. We explore two different observing strategies, (a) taking deep images (e.g., with HST) on small fields, and (b) using shallower images on larger fields.

From these simulations we find that σ_* can be determined to $\lesssim 10\%$ accuracy if a sample of about 5000 galaxies with measured ellipticities are available, down to $R \lesssim 23$. The corresponding data can be obtained on a 4-meter class telescope in a few nights of very good seeing. Alternatively, the same accuracy in the determination of σ_* can be achieved from about ten, moderately deep WFPC2 fields, on which galaxy shapes can be measured to about $R \sim 25$ and for which ground-based images are available on which the WFPC2 fields are centered. Firm lower limits can be set on the radial extent of the halo, but the maximal halo extent is poorly constrained. We show that the likelihood approach can also be used to constrain other parameters of the galaxy population, such as the Tully-Fischer index, or the mean redshift of the galaxies as a function of apparent magnitude. Finally we show how multi-color information, constraining the redshift of individual galaxies, can dramatically improve the accuracy of the parameter determination.

1 Introduction

The distortion of distant source images by the gravitational field of mass concentrations close to their line-of-sight has long been recognized as a powerful tool for studying the distribution of (dark) matter in the universe on various scales (e.g., Kristian 1967; Blandford & Jaroszyński 1981; Webster 1985; Blandford et al. 1991; Kaiser 1992). In particular, the distortion of faint galaxy images by foreground clusters, either in forming arcs or arclets (see the recent review by Fort & Mellier 1994) or by using weaker distortions (Tyson, Valdes & Wenk 1990; Kaiser & Squires 1993) has recently been used to investigate the projected mass distribution of selected clusters of galaxies (Bonnet, Mellier & Fort 1994; Fahlman et al. 1994; Smail et al. 1995; Seitz et al. 1995; Squires et al. 1995) or to detect otherwise unseen mass concentrations (Bonnet et al. 1993; Fort et al. 1995). Distortions due to larger-scale mass distributions have not yet been detected at a highly significant level (Mould et al. 1994), though a possible detection has been reported by Villumsen (1995).

In this paper we explore how to best probe the mass distribution in isolated foreground galaxies through the lensing distortion of background galaxy images. For the idealized case of an isolated, isothermal halo (with critical radius θ_{cr}) this distortion is merely a small stretching (by $\theta_{\text{cr}}/\theta$) of the background image at separation θ , perpendicular to the line connecting the source-lens pair. The distortion caused by a single galaxy cannot be detected, unless its velocity dispersion were greater than about $\sigma \sim 400 \text{ km/s}$ (Mirald-Escudé 1991; Schneider & Seitz 1995), but the statistics of many foreground – background pairs should yield a detectable signal. Tyson et al. (1984) were the first to search for this effect, but failed to detect it. They translated their result into an upper bound for the mass and extent of halos around L_* -galaxies, which was revised upward significantly by Kovner & Milgrom (1987) in a more realistic analysis of the observational results. Tyson et al.'s non-detection, despite the very large number of galaxy images, apparently discouraged other attempts for a decade. However, Brainerd, Blandford & Smail (1995; henceforth BBS) have now discovered a significant galaxy-galaxy lensing signal (at the 99% confidence level) in the data of Mould et al. (1994). The effect was found by considering the statistical distribution of the angle between the line connecting foreground-background pairs and the major axis of the background galaxy. BBS considered pair separations between and $5''$ and $34''$ and split their sample at $m_r = 23$, calling brighter galaxies 'foreground' and fainter ones 'background' objects. They then performed detailed Monte-Carlo simulations resembling their data, using a parameterized model for the galaxy population (see Sect. 2 below), to verify that the observed alignment statistics is compatible with expectations from their galaxy model.

The two most important parameters describing a galaxy halo are its mass (or velocity dispersion, σ) and its radial extent. In the local universe, rotation curves of spiral galaxies suggest the presence of a dark halo with roughly isothermal profile, but little is known about the mass density of galaxies beyond $\sim 30 \text{ kpc}$ (see Zaritsky & White 1994 for the exception). Galaxy-galaxy lensing can in principle probe the size of galactic halos. However, the angular extent of a halo of size $\sim 100 \text{ kpc}$ is considerably larger than the mean angular separation of two 'foreground' galaxies; therefore, more than one lensing galaxy will be important for the distortion of a background image (see the description of the role of multiple deflectors in BBS). Hence, in order to probe large halo sizes, a statistical analysis must be employed which accounts for collective effects. Finally, though

the magnitude of a galaxy is correlated with its redshift, ordering of galaxy distances by their magnitudes is only a rough approximation. By fitting alignment curves through their observational data, BBS accounted for all these effects properly. However, they did not attempt to fit model parameters of their galaxy population to their data.

Here we suggest a new and efficient statistical method for analyzing data on galaxy-galaxy lensing. Its decisive advantage over previous methods lies in the fact that it exploits all the information of the *actual* image configuration (each model predicting the shear for each individual galaxy image) rather than using only the ensemble properties (*e.g.* the mean tangential alignment of major axes) of statistically equivalent samples. It is a maximum-likelihood method which uses the magnitudes, angular positions, and ellipticities of galaxy images as input values. The redshift probability distribution of the galaxies, $p_z(z|m)$, is assumed to be known as a function of apparent magnitude; from redshift surveys, this can be measured for relatively bright galaxies and can be reasonably extrapolated to slightly fainter magnitudes (in fact, we will show that this redshift distribution can be constrained from galaxy-galaxy lensing). One can then calculate for each galaxy image the expectation value of the shear and its dispersion. This shear, combined with the intrinsic ellipticity distribution of the sources, predicts the probability distribution for the observed ellipticities. These are used to calculate the likelihood function, which is then maximized with respect to the parameters of interest. This method is described in detail in Sect. 2. We then generate synthetic data samples, as described in Sect. 3 to which we apply the maximum-likelihood analysis. In most cases, we are interested in the velocity dispersion σ_* and the size s_* of an L_* -galaxy. With only moderately large data sets (which should become available very soon), either on fairly small fields but going deep (*e.g.*, a collection of WFPC2 exposures), or wide-angle field images of moderate depth, σ_* can be determined very accurately, and lower limits on s_* can be derived. As argued above, it is much more difficult to obtain upper bounds on s_* . We then investigate whether the of the results for σ_* and s_* depend sensitively on the knowledge of other galaxy properties, such as the Tully-Fischer index, or the mean redshift as a function of apparent magnitude. We find that these covariances are not very strong and that in fact these additional parameters can be significantly constrained with the maximum-likelihood method. We demonstrate that even an approximate knowledge of the individual galaxy redshifts improve the accuracy of the results considerably; sufficiently accurate redshifts can be obtained from multicolor photometry (Connolly et al. 1995). We discuss our results in Sect. 5, in view of the fact that large data sets useful for our method of analysis will soon become available, due to the increasing number of useful WFPC2 exposures, and the new generation of 10m-class telescopes and wide-field cameras.

2 Method of analysis

In this section we describe the statistical methods for the analysis of galaxy-galaxy lensing. The basic strategy is outlined in Sect. 2.1, and more specific assumptions are given in Sect. 2.2.

2.1 The strategy

We assume that the imaging data available are derived from a single field, and consist of the locations θ_i , and the magnitudes m_i , $1 \leq i \leq N_g$, of N_g galaxies brighter than some threshold m_{lim} . Furthermore, we assume that the ellipticities ϵ_i are measured for a subset of the galaxies, e.g., for all galaxies brighter than some magnitude m_{shape} . (We will refer to this subset as ‘galaxies with shape information’.) Throughout this paper, we use the ellipticity parameter ϵ , which is a complex number with phase 2φ , where φ describes its orientation, and with an absolute value which for an elliptical source with axis ratio $r \leq 1$ is $|\epsilon| = (1 - r)/(1 + r)$. In general, ϵ must be calculated from the second brightness moments of a galaxy image; see, e.g., Schneider (1995) and references therein. The observed ellipticities reflect the intrinsic surface brightness distribution of the sources, modified slightly by the shear induced by gravitational deflection. Galaxy-galaxy lensing tries to infer the latter contribution from the observations in order to put constraints on the deflecting mass distribution.

Obviously, we can only consider contributions to the light deflection from the detected galaxies in the field; later, we will comment on contributions from fainter (unobserved) galaxies, and from larger scale mass distributions like cosmological shear or clusters of galaxies. We also ignore possible effects of all galaxies beyond θ_{max} from any given galaxy image. If we knew the redshifts of all the galaxies and had a model for their (halo) mass distribution, we could predict the lensing shear exactly for each galaxy with shape information and thus reconstruct the intrinsic ellipticity. Requiring that the intrinsic ellipticities are randomly oriented can then constrain the parameters of the (lensing) mass model. This basic strategy will now be outlined in more detail.

We consider only galaxies with shape information that lie at least θ_{max} away from the field boundary. For those images we can predict the shear by summing up the shear contributions from all the galaxies within a circle of angular radius θ_{max} :

$$\gamma_i = \sum_{z_j < z_i} \gamma_{ij} \quad , \quad (2.1)$$

where γ_i is the shear at the i -th galaxy image, obtained by summing the shear contributions γ_{ij} from all galaxies with redshift z_j smaller than z_i . The straight sum in (2.1) is not an exact expression for the resulting shear, as the shear contributions from multiple gravitational deflections do not add linearly (e.g., Blandford & Narayan 1986, Schneider, Ehlers & Falco 1992 – hereafter SEF, Chap. 9). But in the case considered here all shear contributions will be small and the approximation (2.1) applies. The shear, γ , is taken as a complex number, using the same notation as in Schneider (1995). Unfortunately, even for a given mass model of the galaxies, the sum in (2.1) cannot be performed, because we do not know the redshifts of all galaxies. Instead we assign a redshift probability distribution $p_z(z|m)$ to galaxies of a given magnitude m and calculate the expectation value $\langle \gamma_i \rangle$ for the shear of the i -th galaxy. This average requires integrations over the

projected (physical) separations and redshifts and cannot be performed analytically, even for the simplest mass distributions. Such averaging is best performed by Monte-Carlo integration: for each galaxy in the data field we draw a redshift z_i from the distribution $p_z(z|m_i)$ and calculate for each galaxy with shape information the shear γ_i from (2.1). Repeating this process N_{MC} times, the mean shear and its dispersion,

$$\langle \gamma_i \rangle = \frac{1}{N_{\text{MC}}} \sum_{\nu=1}^{N_{\text{MC}}} \gamma_i^\nu$$

and $\sigma_{\gamma,i}^2 = \langle (\gamma_i - \langle \gamma_i \rangle)^2 \rangle$ can be calculated.

Let $p^{(\text{s})}(\epsilon^{(\text{s})}) d^2\epsilon^{(\text{s})}$ be the probability that the intrinsic (complex) ellipticity of a galaxy lies within $d^2\epsilon^{(\text{s})}$ of $\epsilon^{(\text{s})}$. This ellipticity distribution might depend on the redshift and brightness of the galaxies, or on its color. For simplicity we assume here that this distribution is the same for all galaxies. For weak shear, the relation between intrinsic ellipticity and observed ellipticity is approximately

$$\epsilon = \epsilon^{(\text{s})} - \gamma \quad , \quad (2.2)$$

so that the probability density for the observed ellipticity reads

$$p_\epsilon(\epsilon|\gamma) = p^{(\text{s})}(\epsilon + \gamma) \quad . \quad (2.3)$$

From the Monte-Carlo integration, which for each realization of the galaxy redshifts yields a value γ_i^ν , the effective ellipticity probability distribution is a mean of (2.3) over all realizations,

$$\langle p_i \rangle(\epsilon_i) = \frac{1}{N_{\text{MC}}} \sum_{\nu=1}^{N_{\text{MC}}} p^{(\text{s})}(\epsilon_i + \gamma_i^\nu) \quad . \quad (2.4)$$

From these probability densities, we can now construct the likelihood function

$$\mathcal{L} = \prod_i \langle p_i \rangle(\epsilon_i) \quad , \quad (2.5)$$

where the product extends over all galaxy images with shape information. Maximizing this likelihood function with respect to the model parameters yields their best fitting values.

2.2 Specific assumptions

To carry out the program outlined in the preceding subsection, we have to provide a parametrized description of the galaxy population. In this parametrization, we follow essentially the description given in BBS.

Number counts – magnitude relation. We assume that the number counts of galaxies follow a power-law distribution of the form

$$\frac{d \log N(m)}{dm} \propto 10^{\gamma m} \quad , \quad (2.6)$$

where the slope γ depends on the waveband used and can be determined empirically. Note that we need this distribution function only for generating the synthetic data set, as described in Sect. 3; it is not used in the maximum likelihood analysis.

Redshift distribution. Following BBS, we assume that the redshift distribution of the galaxies is given as

$$p_z(z|m) = \frac{\beta z^2 \exp(-(z/z_0)^\beta)}{\Gamma(3/\beta) z_0^3} , \quad (2.7a)$$

where $\Gamma(x)$ is the gamma function, and $z_0(m)$ is assumed to depend linearly on the apparent magnitude of the galaxies,

$$z_0 = k_z [z_m + z'_m(m - 22)] , \quad (2.7b)$$

where k_z , z_m and z'_m are constants.

Lens model. As in BBS, we describe the mass distribution of the galaxies by the axially-symmetric surface mass density

$$\Sigma(\xi) = \frac{\sigma^2}{2G\xi} \left(1 - \frac{\xi}{\sqrt{s^2 + \xi^2}} \right) , \quad (2.8)$$

which corresponds to a singular isothermal sphere with characteristic outer scale s . We will assume that s scales quadratically with σ ,

$$s = s_* \left(\frac{\sigma}{\sigma_*} \right)^2 =: s \hat{\sigma}^2 , \quad (2.9)$$

where σ_* is the velocity dispersion of an L_* -galaxy. Using the notation of SEF, we obtain for the dimensionless surface mass density κ of a galaxy at redshift z_d for a source at redshift z_s :

$$\kappa(\theta) = 4\pi \left(\frac{\sigma_*}{c} \right)^2 \hat{\sigma}^2 \frac{r_{ds}}{r_s} \frac{1}{2\theta} \left(1 - \frac{\theta}{\sqrt{\theta^2 + \theta_s^2}} \right) , \quad (2.10)$$

where the r -factors are angular-diameter distances in units of c/H_0 , θ is the angular separation of the source image from the center of the potential, and

$$\theta_s = \frac{s}{r_{dc}/H_0} .$$

Defining

$$\theta_t = \frac{s_*}{(c/H_0)} , \quad (2.11)$$

one obtains

$$\theta_s = \frac{\hat{\sigma}^2 \theta_t}{r_d} . \quad (2.12)$$

From Eq. (8.15) of SEF, the modulus of the shear is

$$|\gamma| = 4\pi \left(\frac{\sigma_*}{c} \right)^2 \hat{\sigma}^2 \frac{r_{ds}}{r_s} \left(\frac{2\theta_t + \theta}{2\theta^2} - \frac{\theta^2 + 2\theta_t^2}{2\theta^2 \sqrt{\theta^2 + \theta_t^2}} \right) , \quad (2.13)$$

and the phase of γ is determined by the direction of the background galaxy image relative to the deflector center. Throughout this paper we assume an Einstein-de Sitter universe, for which

$$\begin{aligned} r_d &= \frac{2}{1+z_d} \left(1 - \frac{1}{\sqrt{1+z_d}} \right) \quad , \\ \frac{r_{ds}}{r_s} &= \frac{\sqrt{1+z_s} - \sqrt{1+z_d}}{(\sqrt{1+z_s} - 1) \sqrt{1+z_d}} \quad . \end{aligned} \quad (2.14)$$

Velocity dispersion – luminosity relation. To link the dynamical halo properties to the observable galaxy luminosity, we use a Faber–Jackson / Tully–Fischer type relation of the form

$$\frac{L}{L_*} = \left(\frac{\sigma}{\sigma_*} \right)^\eta \quad . \quad (2.15)$$

Luminosity-magnitude relation. Again following BBS, we shall take

$$\frac{L}{L_*} = r_d^2 (1+z)^{3+\alpha} 10^{0.4(23.9-m)} \quad , \quad (2.16)$$

where the numerical value in the exponent was chosen to apply to photometry in the red band, and α accounts for the k-correction.

Intrinsic ellipticity distribution. The intrinsic ellipticity distribution of galaxies can be determined in principle from high-resolution imaging; for example, the HST Medium Deep Survey will most likely provide an accurate description of the intrinsic ellipticity distribution. In this paper, we shall for simplicity assume a distribution of the form

$$p^{(s)}(\epsilon^{(s)}) = \frac{1}{\pi \rho^2} \exp \left(-\frac{|\epsilon^{(s)}|^2}{\rho^2} \right) \quad . \quad (2.17)$$

Then the averaged probability distribution for the observed ellipticities becomes

$$\langle p_i \rangle(\epsilon_i) = \frac{1}{\pi \rho^2 N_{\text{MC}}} \sum_{\nu=1}^{N_{\text{MC}}} \exp \left(-\frac{|\epsilon_i + \gamma_i^\nu|^2}{\rho^2} \right) \quad . \quad (2.18)$$

Since the shear will be small, the resulting probability distribution will again approximately be a Gaussian,

$$\langle p_i \rangle(\epsilon_i) = \frac{1}{\pi (\rho^2 + \sigma_{\gamma,i}^2)} \exp \left(-\frac{|\epsilon_i + \langle \gamma_i \rangle|^2}{\rho^2 + \sigma_{\gamma,i}^2} \right) \quad , \quad (2.19)$$

in which case the log-likelihood function takes the form

$$\ell := \ln \mathcal{L} = - \sum_i \frac{|\epsilon_i + \langle \gamma_i \rangle|^2}{\rho^2 + \sigma_{\gamma,i}^2} - \sum_i \ln [\pi (\rho^2 + \sigma_{\gamma,i}^2)] \quad . \quad (2.20)$$

If ℓ_{\max} is the maximum value of the log-likelihood, then the probability distribution of $2(\ell_{\max} - \ell)$ follows approximately a χ^2 distribution with the numbers of degrees freedom equal to the number of varied model parameters.

Fiducial values of the parameters. Some of the parameters necessary to specify the various distributions can be easily determined from existing or forthcoming observations, and are thus not critical. For example, the ellipticity distribution of the source images will become known very soon. Unless noted otherwise, we shall use the following values of the parameters: $\alpha = 3$, $\eta = 4$, $\beta = 1.5$, $k_z = 0.7$, $z_m = 0.47$, $z'_m = 0.1$, $\rho = 0.2$.

3 Simulations

The subsequent simulations are done by distributing the galaxies in a single quadratic field of sidelength θ_{field} . Again, galaxies with shape information are only considered in the likelihood function if they are at least θ_{\max} from the the field boundary. It is clear that the method does not require a single contiguous field; what matters is the number of galaxies with shape information for which the location of surrounding galaxies (within θ_{\max}) are known. For example, one could consider a number of WFPC2 fields for which ground-based images are available on which the WFPC2 field is centered; this would yield essentially equivalent information as the one synthetically generated here.

The test of the maximum likelihood algorithm consists of two steps, (1) the generation of “data”, drawn from an input model for the galaxy population, and (2) the estimate of the input parameters by calculating the relative likelihoods of different retrieving models. In the simulations we generate data by distributing galaxies over a quadratic field of size $\theta_{\text{field}} + 2\theta'_{\max}$, with a magnitude distribution of the form (2.6), and with $\gamma = 0.3$, such that the surface number density of galaxies is 70/sq.arcmin ($m \leq 26$, Smail *et al.* 1995). The galaxies are distributed in the magnitude interval $m \in [20, 26]$, and are assigned a redshift according to the distribution (2.7). We take $\theta'_{\max} = 5$ arcmin. We choose a set of input values for σ_* and s_* , σ_*^{in} and s_*^{in} , calculate the shear from (2.1) for each galaxy within the square of size θ_{field} and draw an intrinsic ellipticity from the probability distribution (2.17). From (2.2) the observed ellipticity of each galaxy is then calculated and stored along with the angular positions and magnitudes of the galaxies.

To retrieve the input parameters σ_*^{in} and s_*^{in} for the lens model, we proceed as described in the previous section. We assume that galaxies brighter than m_{shape} carry shape information and that all galaxies brighter than m_{lim} are observed. We perform the likelihood analysis for all galaxies with shape information inside the square of size $\theta_{\text{field}} - 2\theta_{\max}$ which have no observed galaxy closer than θ_{\min} , since for those the ellipticity will be difficult to obtain. For the Monte-Carlo integration of $\langle \gamma_i \rangle$, typically $N_{\text{MC}} = 20$ is sufficient. For all simulations presented in this paper, we choose $\sigma_*^{\text{in}} = 160$ km/s and $s_*^{\text{in}} = 80h^{-1}$ kpc, where h is the Hubble constant in units of 100 km/s/Mpc.

4 Results

In the analysis at hand two sources of uncertainty must be considered: First, purely statistical errors caused by the incompleteness of the information available. In principle, these errors can always be decreased by using larger and larger data sets. Second, even with unlimited data one may arrive at the “wrong answer”, if the input model (or nature) is not included in the space spanned by the models used in the likelihood analysis. These two effects will be investigated in turn in Sections 4.1 and 4.2. Finally, we shall demonstrate in Sect. 4.3 how much better σ_*^{in} and s_*^{in} can be reconstructed, if approximate redshifts ($\Delta z \sim 0.05$) for the galaxies are available.

4.1 Correct model assumptions

Fig. 1 shows the results of the likelihood analysis, for different assumptions about the amount and the quality of the available data. Contours of constant log-likelihood ℓ as a function of the trial parameters s_* and σ_* in the reconstruction are displayed. The four panels represent results for two different threshold magnitudes m_{shape} and data field sizes θ_{field} .

For all parameters the log-likelihood function has a broad maximum (X), which is elongated in the direction of s_* , because s_* is much less well determined than σ_* . Note that a difference of $\ell_{\text{max}} - \ell = 1, 2, 3$ corresponds to a confidence level of $p = 63\%, 86\%, 95\%$, respectively, implying that the retrieved parameter values at the likelihood maximum are statistically consistent with the input value of (s_*, σ_*) . The figure also shows that the upper bound on s_* is unconstrained in these particular simulations, but that significant lower bounds on s_* can be obtained for three out of four cases. In addition, Figure 1 illustrates that the velocity dispersion σ_* is well constrained by this method. As expected, the accuracy with which the model parameters can be derived increases dramatically with the number of galaxy images used for the analysis.

Each panel in Figure 1 shows the results for one particular realization of the data set. To determine how well, on average, the lens parameters σ_* and s_* can be determined, the analysis shown in each panel should be repeated with other data realizations, producing many likelihood maps. To present all this information we resort to the following approach: for any assumed value of s_* , one can determine the value of σ_* which maximizes the likelihood function, denoted by $\hat{\sigma}_*(s_*)$. The set $\hat{\sigma}_*(s_*)$ traces a curve in the (s_*, σ_*) -plane, which contains the best fit values of (s_*, σ_*) for the given data set. For the same parameters as those used in Fig. 1, we have calculated these curves for ten realizations of the galaxy distribution; they are plotted in Fig. 2.

Although this figure appears crowded, it is worthwhile to discuss it in some detail. As an example, consider the upper right panel. In all ten cases, the maximum of the likelihood is attained at values of σ_* (filled hexagons) which are less than ~ 25 km/s away from the input value of 160 km/s. In fact, in eight of these ten cases, the difference of the best fit value from the input value is less than 10 km/s. The value of s_* is not well constrained, as was already clear from the contour maps in Fig. 1. On the other hand, in all ten cases can a lower limit on s_* be determined. The points on the $\hat{\sigma}_*(s_*)$ curves where $\ell_{\text{max}} - \ell = 1, 2, 3$ are marked with triangles, stars, and squares, respectively. In none of the ten cases does the 68% lower limit of s_* lie above the true value of s_* . In seven (six) cases, even 86% (95%) confidence upper limits can be obtained. The figure furthermore shows that the information which can be extracted from a synthetic data

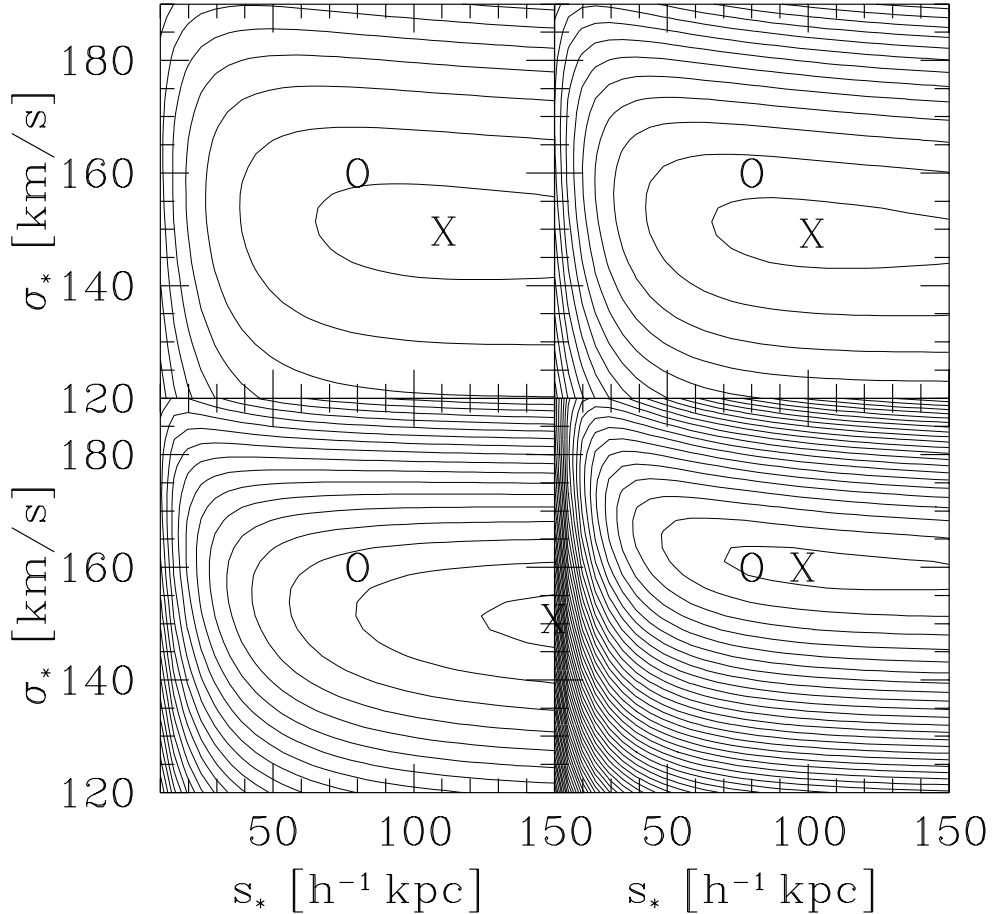


Fig. 1. Log-likelihood contours in the s_* - σ_* plane, for $\theta_{\text{field}} = 10'$ (two upper panels) and $\theta_{\text{field}} = 15'$ (lower panels). In the left panels, $m_{\text{shape}} = 24$, in the right panels $m_{\text{shape}} = 24.5$. The number of galaxies whose shape information has been used, i.e., which are brighter than m_{shape} , have no ‘visible’ galaxy inside $\theta_{\min} = 3''$, and are at least $\theta_{\max} = 1'$ away from the boundary of the field, is 795 (upper left panel), 1165 (upper right panel), 2169 (lower left panel), and 3137 (lower right panel). All galaxies brighter than $m_{\text{lim}} = 25$ are taken into account for calculating the mean shear $\langle \gamma_i \rangle$ and its dispersion $\sigma_{\gamma, i}$ according to (2.1). The contours in this and the following contour plots are $\ell_{\max} - \ell = 0.1, 0.5, 1, 1.5, \dots$. The O marks the input values of the parameters ($s_*^{\text{in}} = 80 h^{-1} \text{ kpc}$, $\sigma_*^{\text{in}} = 160 \text{ km/s}$), and X denotes the position of the maximum of the likelihood function inside the displayed parameter space

set varies from realization to realization, but that the significance of the values obtained can be extracted from the data by our statistical approach.

The decrease of $\hat{\sigma}_*(s_*)$ with s_* shows that the best-determined value from the likelihood analysis is a mass estimate. The mass of an L_* -galaxy within a projected radius ξ is

$$M(< \xi) = \frac{\pi \sigma_*^2}{2G} [s_* + \xi - \sqrt{s_*^2 + \xi^2}] \quad . \quad (4.1)$$

One can now insert the value $\hat{\sigma}_*^2(s_*)$ into this mass formula, which yields $M(< \xi)$ as a function of s_* . It turns out that for the cases shown in Figs. 1 and 2 this curve is fairly flat for $\xi \sim 10 h^{-1} \text{ kpc}$, and that the corresponding values of $M(< \xi)$ lie within $\sim 15\%$

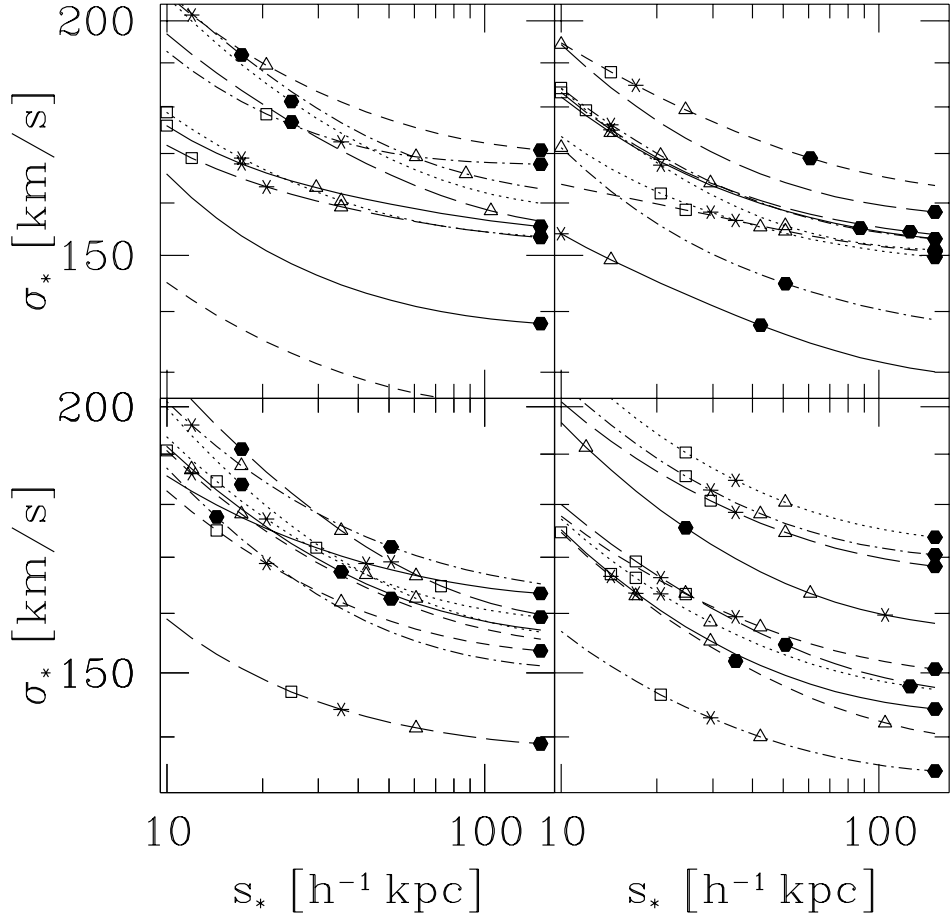


Fig. 2. The value $\hat{\sigma}_*(s_*)$ which maximizes the likelihood for a fixed value of s_* is plotted for ten different realizations of the galaxy distribution. The parameters for each panel are the same as the corresponding ones in Fig. 1. The filled hexagon on each curve denotes the point where the likelihood attains its maximum, within the range $10h^{-1}\text{kpc} \leq s_* \leq 150h^{-1}\text{kpc}$. In the upper left panel, the lowest (dashed) curve attains its minimum of the likelihood at $\sigma_* = 124 \text{ km/s}$. The triangles, stars, and squares correspond to points on the curves where $\ell_{\max} - \ell(s_*, \hat{\sigma}_*) = 1, 2, 3$, respectively

of the true value. Note that $10h^{-1}\text{kpc}$ corresponds to about $\theta_{\min} = 3''$ for a galaxy at a typical redshift of 0.4.

In order to investigate the dependence of the results on the two scales θ_{\min} and θ_{\max} , we have plotted in Fig. 3 the likelihood contours for the same parameters as in the upper right panel of Fig. 1, except that we changed the values of θ_{\min} and θ_{\max} .

For the same value of θ_{\min} and the same data field size, the difference between the two right and the two left panels in Fig. 3 lies in an increase of θ_{\max} . This has two effects: for each image with shape information the number of potential lenses considered increases and so does the information used in the likelihood analysis. On the other hand, the increase in θ_{\max} reduces the area where galaxy images with shape information are far enough from the field edge to be considered in the analysis; this reduces N . As can be seen from the figure, the second effect dominates the first one, reiterating the importance of

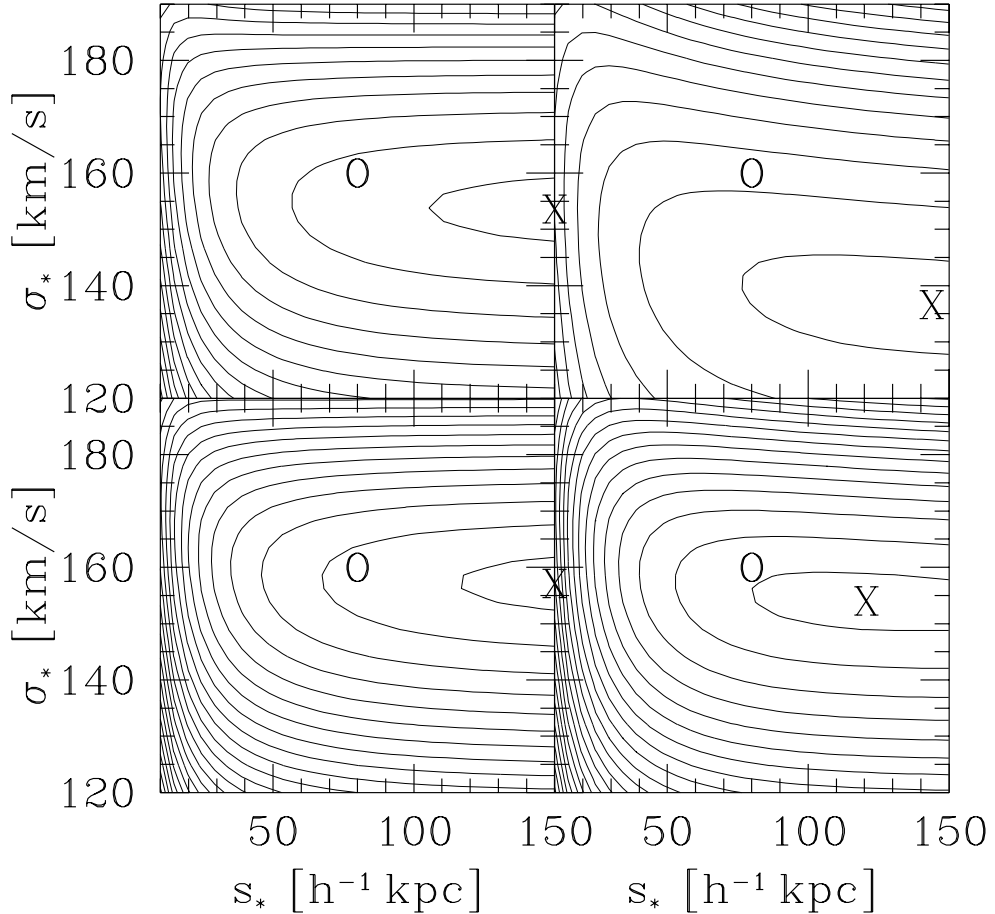


Fig. 3. Same as Fig. 1, for the same parameters as those of the upper right panel of Fig. 1, i.e., $\theta_{\text{field}} = 10'$ and $m_{\text{shape}} = 24.5$, except that the inner and outer radii are varied: upper left panel: $\theta_{\min} = 3''$, $\theta_{\max} = 30''$, number of galaxies with shape information used, $N = 1471$; upper right panel: $\theta_{\min} = 3''$, $\theta_{\max} = 120''$, $N = 633$; lower left panel: $\theta_{\min} = 2''$, $\theta_{\max} = 30''$, $N = 1728$; lower right panel: $\theta_{\min} = 2''$, $\theta_{\max} = 60''$, $N = 1366$. As before, the O marks the input values of the parameters ($s_*^{\text{in}} = 80h^{-1} \text{ kpc}$, $\sigma_*^{\text{in}} = 160 \text{ km/s}$), and X denotes the position of the maximum of the likelihood function

the total galaxy image number on the accuracy of the results. In addition, the reduction of θ_{\min} in the lower two panels leads to a increase of accuracy in the determination of σ_* .

Possible Applications.

In the following we will consider two specific types of data sets to constrain the lens parameters s_* and σ_* : (1) HST images, where the ellipticities can be measured accurately for fairly faint and small galaxies, i.e., where the number density of galaxies with shape information is high. (2) Ground-based images, where the limit for shape measurements is brighter, but where the reduced galaxy density can be compensated by observations over a larger area on the sky.

Deep Images / Small Fields

For the case (1) we consider, as before, a galaxy distribution with 70 objects per square arcminute ($20 \leq m \leq 26$) and the same input parameters as above. We assume that the faint galaxies with shape information come from a $7' \times 7'$ region, corresponding to about 10 WFPC2 fields. In the following we choose $\theta_{\text{field}} = 7' + 2\theta_{\text{max}}$, assuming that the HST images will be supplemented by ground-based data, which cover a larger area than the WFPC2 field. Such data would provide shape and photometric information for all galaxies in the WFPC2 field with $m < m_{\text{shape}}$; the ground-based data provide photometric information for galaxies brighter than m_{lim} , which might be brighter than m_{shape} . Those galaxies brighter than m_{lim} within θ_{max} are then used in the likelihood analysis, as before.

In Fig. 4 we have plotted the log-likelihood contours in the (s_*, σ_*) -plane, for several combinations of θ_{min} , θ_{max} , m_{shape} and m_{lim} . The synthetic galaxy catalog is the same for all eight panels with the same value of θ_{max} . Several general trends can be deduced: (1) decreasing θ_{min} yields a better defined likelihood maximum, because tight source-lens pairs yield more information about σ_* than more distant pairs. (2) Considering fainter galaxies as potential lenses (*i.e.* increasing m_{lim}) does not improve the constraints on s_* and σ_* , since these fainter galaxies are mainly at redshifts beyond the source galaxies'. (3) going to fainter limits of m_{shape} , however, provides tighter parameter constraints by increasing the number of galaxies with shape information. (4) an increase of the radius θ_{max} , within which potential lenses are considered, improves the lower limits on the halo cut-off s_* . This is intuitive, because only the large-separation pairs can probe the cut-off radius of the mass distribution of the lenses.

For the same combinations of parameters as in Fig. 4, we have repeated the calculation of the log-likelihood function for 30 realizations of the galaxy distribution, and determined the maximum of ℓ as a function of s_* and σ_* . The positions of these maxima are plotted in Fig. 5. As we have seen before, the maximum of the likelihood function can occur at very large values of s_* , since the upper limit on the cut-off radius is not well determined in many cases. In order to display all points in a limited region of the (s_*, σ_*) -plane, we have moved points with $s_* > 200h^{-1}$ kpc somewhat arbitrarily to smaller values of s_* ; these still yield a fairly accurate determination of the σ_* -value of the maximum.

Most importantly, the location of the log-likelihood maximum constitutes a fairly unbiased estimate of σ_* , except for the rare cases where the estimate of s_* is very small. If the location of the maximum of the log-likelihood function occurs at small values of s_* , then these points tend to lie along curves similar to those plotted in Fig. 2, *i.e.*, small values of s_* correspond to large values of σ_* . As we have discussed above, if the radius θ_{max} within which potential lenses are considered is increased, small estimates of s_* do no longer occur, *i.e.*, much better lower limits on s_* can be obtained. Furthermore we see that the scatter of points in Fig. 5 is reduced when θ_{min} is decreased and m_{shape} is increased.

Less Deep Imaging / Wide Fields

We next consider the case of data on a large angular field, but with a brighter limiting magnitude. This case is more appropriate for ground-based images, where the atmospheric effects limit the accuracy with which ellipticities of faint and small galaxy images can be measured. A galaxy distribution was simulated on a field of size $(40')^2$

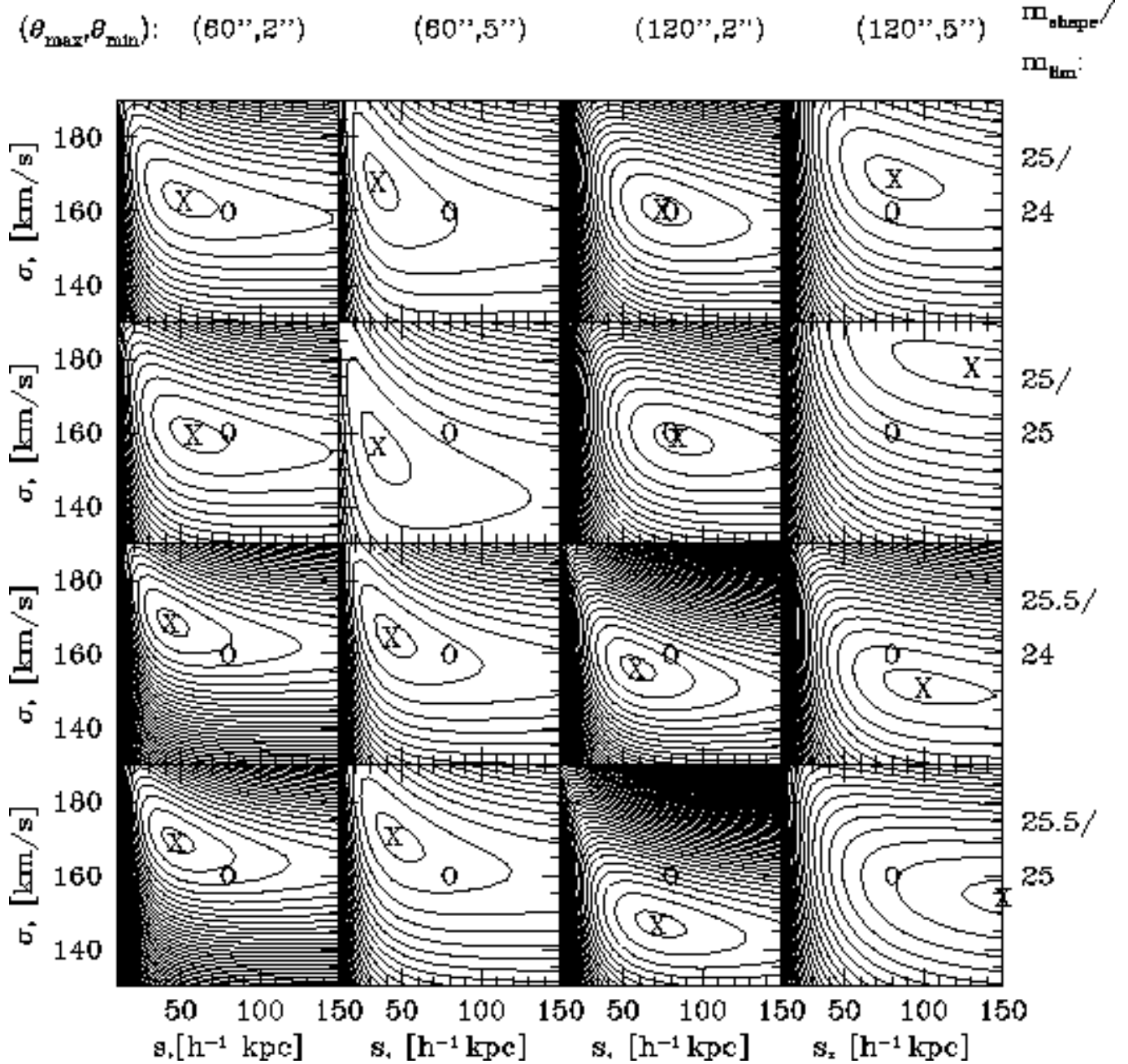


Fig. 4. Log-likelihood contours, as in Fig. 1, for a particular realization of the galaxy distribution, for different combinations of the parameter θ_{\min} , θ_{\max} , m_{shape} and m_{lim} , as indicated. Again, X denotes the maximum of the log-likelihood, O denotes the input model values. In all cases, the solid angle from which galaxies with shape information are taken is 49 sq.arcmin., corresponding to about 10 WFC fields

in the same way as before, i.e., 70 galaxies per sq. arcmin. brighter than $m = 26$ were distributed and the ellipticities calculated. The log-likelihood contours for four combinations of θ_{\min} and m_{shape} are plotted in Fig. 6; in all cases, only galaxies brighter than $m_{\text{lim}} = 24$ were taken into account as potential lenses within $\theta_{\max} = 2'$. Whereas the galaxy sample is considerably shallower than that in Fig. 4, this effect is compensated by the much larger solid angle: in all cases displayed, a good approximation for σ_* is obtained, as well as useful lower bounds on s_* .

To summarize this subsection, we have shown that statistical properties of the galaxy

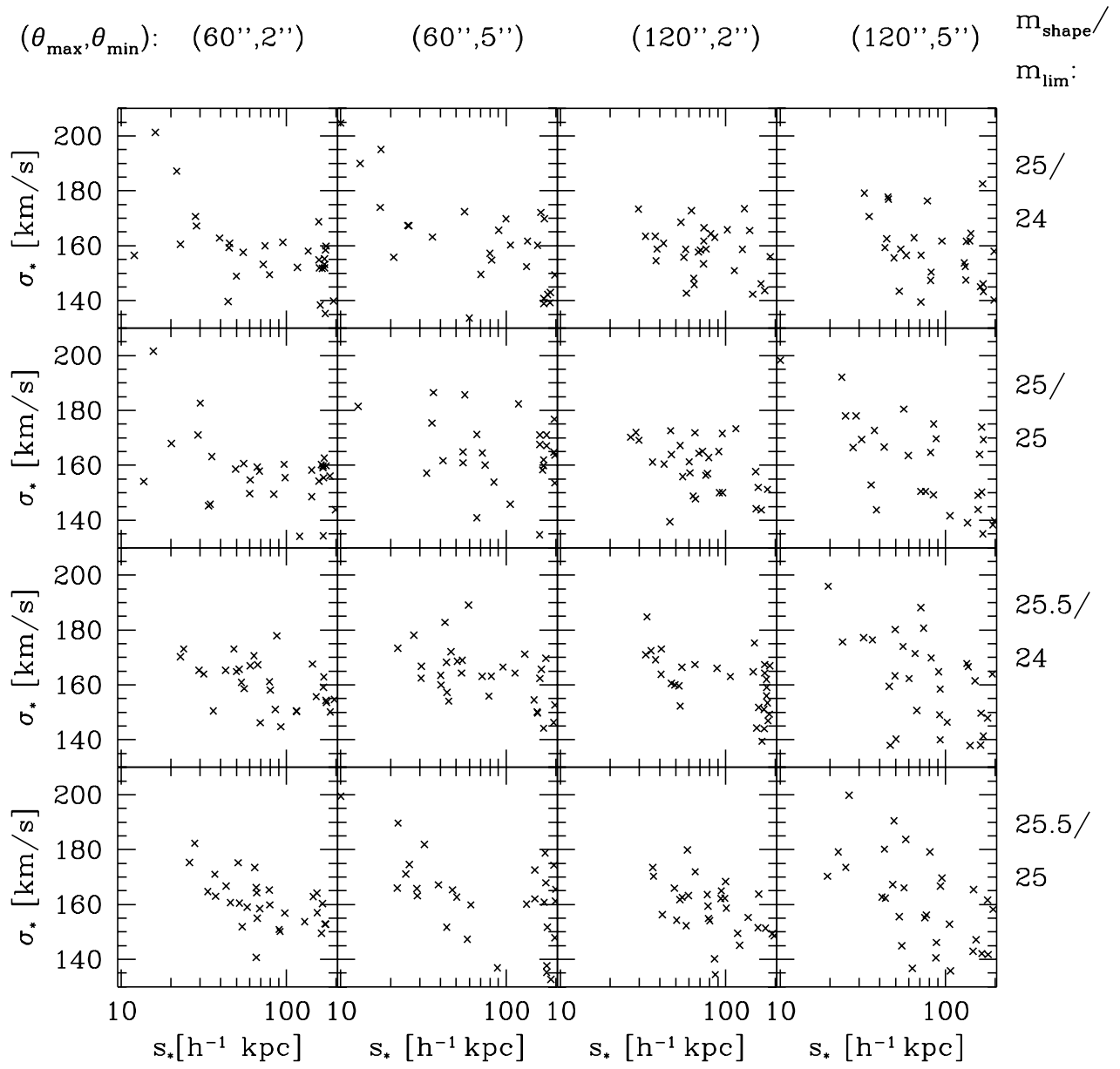


Fig. 5. For different combinations of the parameters θ_{\min} , θ_{\max} , m_{shape} and m_{lim} , as indicated, we have plotted for 30 realizations of the galaxy distribution the best-fitting values for s_* and σ_* , for the same input parameters as before, i.e., $s_*^{\text{in}} = 80h^{-1} \text{ kpc}$, $\sigma_*^{\text{in}} = 160 \text{ km/s}$. Values of $s_* > 150h^{-1} \text{ kpc}$ do not correspond to actual maxima of the log-likelihood function, but are estimates of a lower limit of these maxima, obtained from extrapolations of the likelihood function along curves $\hat{\sigma}_*(s_*)$ such as plotted in Fig. 2

population can be inferred from galaxy-galaxy lensing. Two strategies have been considered in somewhat more detail: deep images of a fairly small field, or shallower images on large fields. In both cases can significant constraints on the values of σ_* and s_* be obtained. However, the information obtained in both cases is not necessarily equivalent, since the deep images may reveal effects of cosmological evolution of the galaxy popula-

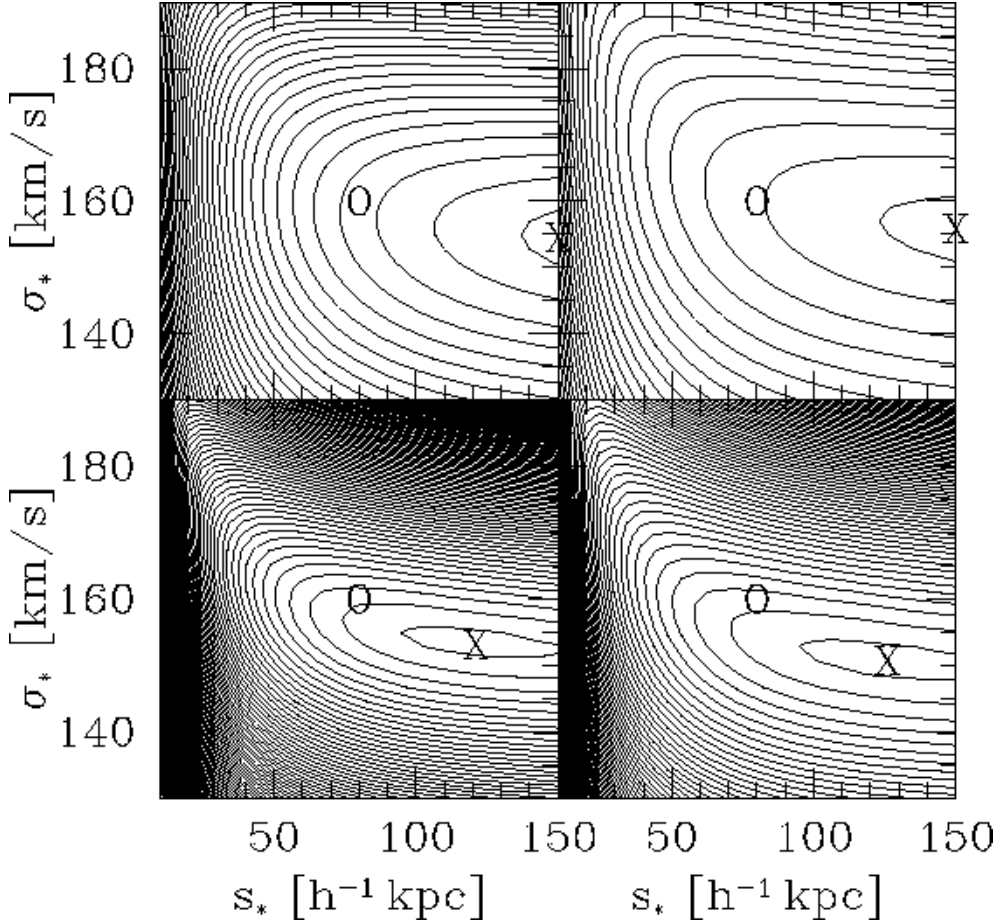


Fig. 6. Log-likelihood contours in the s_* - σ_* plane, for $\theta_{\text{field}} = 40'$. In the upper panels, $m_{\text{shape}} = 22.5$, in the lower panels $m_{\text{shape}} = 23.5$. Only those galaxies without a neighboring galaxy within $\theta_{\min} = 3''$ (left panels) and $\theta_{\min} = 5''$ (right panels) were considered. In all cases, $m_{\text{lim}} = 24$ and $\theta_{\max} = 2'$. The number of galaxies whose shape information has been used is 5891 (upper left panel), 4731 (upper right panel), 12975 (lower left panel), and 10392 (lower right panel)

tion. The fact that our analysis for the cases shown in Fig. 6 yields estimates for σ_* and s_* close to the input values shows that additional galaxies which were not accounted for in our analysis (namely those with $m_{\text{lim}} = 24 \leq m \leq 26$) do not significantly bias the estimate. The analysis here has assumed that the redshift distribution of the galaxies, the Tully-Fisher index, and the k-correction are known precisely. In the next subsection, we shall investigate whether these assumptions are critical, or whether some of these parameters can even be constrained from galaxy-galaxy lensing.

4.2 Variation of the model parameters

Next we consider the consequences of the fact that in practice further parameters of the input model are unknown (not only σ_* and s_*). Instead of trying to cover a large region of parameter space, we will focus on two parameters, the “Tully-Fisher index” η and the parameter z'_m (from Eq. 2.7), which characterizes the change in the mean redshift as a function of apparent magnitude.

We use the same synthetic data as used for Fig. 6, but calculate the likelihood function (2.20) for various values of η and z'_m . For three different values of s_* we specify a grid in η and z'_m and maximize ℓ by varying σ_* (*i.e.* determine $\hat{\sigma}_*$ in the notation used

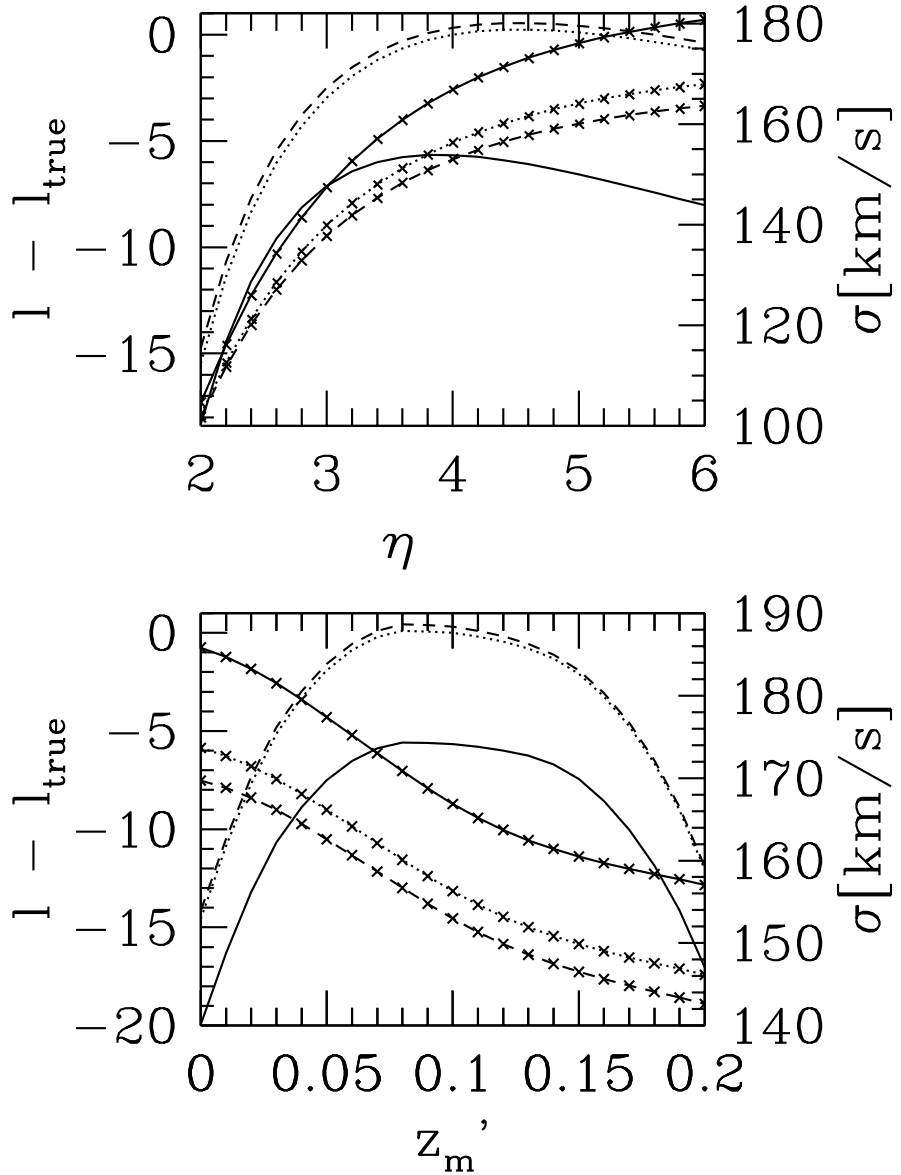


Fig. 7. For the same data as used for Fig. 6, the likelihood was maximized as a function of σ_* , for three values of s_* : $s_* = 30, 80, 130 h^{-1} \text{ kpc}$ (solid, dotted, and dashed curves, respectively). Here, $\theta_{\min} = 3''$, $m_{\text{shape}} = 23.5$, and $m_{\text{lim}} = 24$, i.e., these parameters correspond to the lower left panel in Fig. 6. The likelihood was maximized for various values of the Tully-Fischer index η (upper panel) and the redshift parameter z'_m occurring in eq. (2.7) (lower panel). The curves without crosses display the difference between the log-likelihood of the best-fitting model and the log-likelihood of the input model, i.e., for $\eta = 4$, $z'_m = 0.1$, $s_* = 80 h^{-1} \text{ kpc}$, and $\sigma_* = 160 \text{ km/s}$, whereas the curves with crosses display the corresponding best-fitting value of σ_* .

in Fig. 2). In Fig. 7 we plot the difference $\ell - \ell_{\text{true}}$ between the log-likelihood of a model and its value at the input parameters, as a function of η (upper panel) and as a function of z'_m (lower panel). Also, the corresponding value of σ_* which maximizes ℓ (for fixed s_*) is plotted.

These simulations illustrate a number points. Whereas the log-likelihood curves are fairly flat for values of $\eta \gtrsim 4$, any value $\eta \lesssim 3$ can be excluded from the upper panel

in Fig. 7. In the limit $\eta \rightarrow 0$ all the lensing power would be concentrated in the very brightest galaxies; this can be rejected by this analysis. The weak constraint on $\eta \rightarrow \infty$ does not imply a correspondingly large uncertainty in σ_* , as σ becomes independent of the galaxies' luminosity in this limit.

On the other hand, the log-likelihood function exhibits a pronounced maximum as a function of z'_m , as seen in the lower panel of Fig. 7. The true (input) value is $z'_m = 0.1$, and the allowed range of z'_m is about $0.05 \lesssim z'_m \lesssim 0.15$. The corresponding range in σ_* is then $145 \lesssim \sigma_*/\text{km/s} \lesssim 165$.

We conclude from this that the method for analyzing galaxy-galaxy lensing introduced here is not very sensitive to variations of parameters and that, in fact, the likelihood ratio test can actually constrain the range of model parameters from the data.

4.3 Redshift information

Up to now we have assumed that the apparent magnitude is the only observable which determines the probability distribution of the redshift of a galaxy, using the distribution function (2.7). However, it is conceivable that additional information on the galaxy images can be obtained, most noticeably the color, which might be used to constrain the redshift interval. For example, Connolly et al. (1995) have demonstrated that the redshifts for galaxies with $B_J \leq 22.5$ can be estimated from four-color photometry to an accuracy of $\Delta z \lesssim 0.05$.

We shall now demonstrate that s_* and σ_* can be determined much more accurately, if such redshift estimates are available. Again we use the same data as for Fig. 6, but assume that the redshift of the galaxies have been estimated with a fractional accuracy of ϵ . For simplicity we assume that the redshift of a galaxy lies within the interval $(1 - \epsilon)z_{\text{true}} \leq z \leq (1 + \epsilon)z_{\text{true}}$, of the true redshift. We then use this redshift interval in the Monte-Carlo integration of $\langle \gamma_i \rangle$ and $\sigma_{\gamma,i}^2$ which enter the log-likelihood function (2.20).

In Fig. 8 we have plotted the log-likelihood contours for the same parameters as for the lower right panel of Fig. 6, except that we used the redshift distribution just mentioned, with $\epsilon = 0.05$ (left panel) and $\epsilon = 0.5$ (right panel). For the same number of galaxies the contours are now tighter than those in Fig. 6, i.e., σ_* and a lower limit on s_* can be much better determined if redshift information is included. In fact, in the present case we can actually also determine an upper limit on s_* . The comparison of the two panels in Fig. 8 shows that even an imprecise redshift estimate from multi-color photometry considerably improves the estimates of the lens parameters.

5 Discussion

In this paper we have developed an efficient, quantitative analysis method for galaxy-galaxy lensing, an effect which has been observationally detected by BBS. The method is based on a maximum likelihood approach which accounts for all of the information available from observation. It accounts not only for the image ellipticities, but uses the actual relative positions and magnitudes for all surrounding galaxies which might be potential lenses. From synthetically generated data sets we have shown that our method can be used to determine statistical properties of galaxies, such as the velocity dispersion σ_* of an L_* -galaxy or its characteristic tidal cut-off radius. Even for moderately large

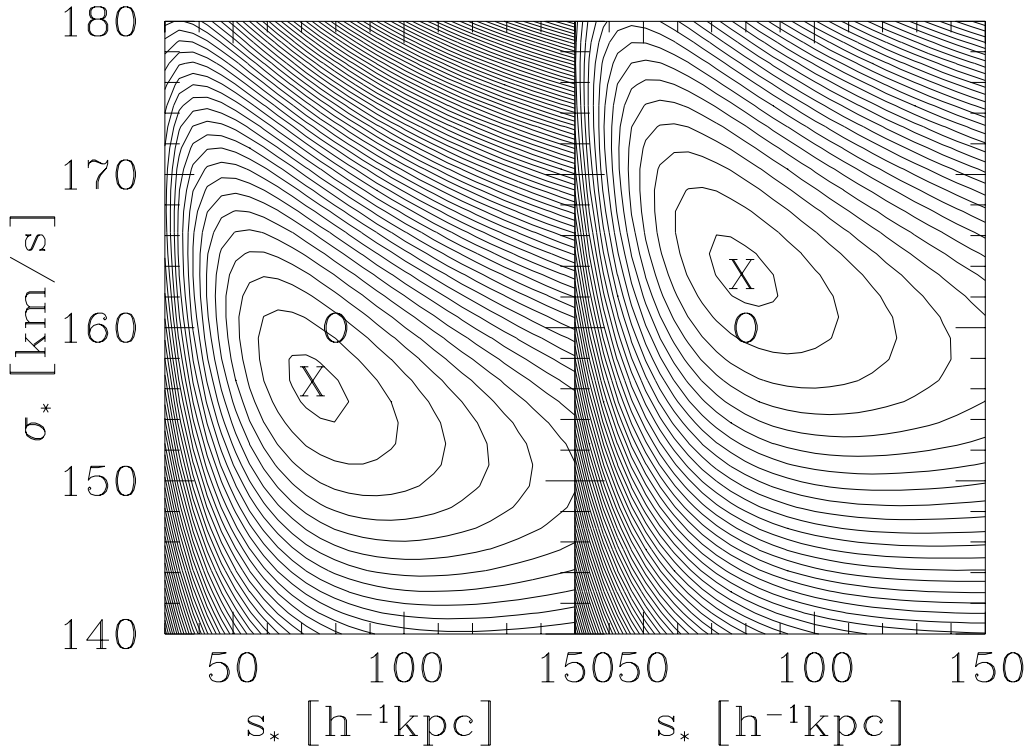


Fig. 8. Log-likelihood contours for the same parameters as for the lower right panel in Fig. 6, i.e., $\theta_{\min} = 5''$, $m_{\text{shape}} = 23.5$, but with ‘redshift information’ as described in the text. The left (right) panel corresponds to $\epsilon = 0.05$ ($\epsilon = 0.5$). Note that the region of the (s_*, σ_*) -plane displayed here is smaller than in the previous figures

galaxy samples, the accuracy of this determination is quite high. For example, with only 10 sufficiently deep WFPC2 images can σ_* be determined with a statistical accuracy of about 10%. Alternatively, high-quality images with a 4-meter class telescopes taken with a non-too-small field-of-view can yield the required galaxy number in a few nights. After all, it seems from our analysis that the requirement on the amount of data is not very demanding, except that the systematic effects which affect the measured ellipticities on ground-based images has to be understood sufficiently well.

We have also demonstrated that other statistical properties of the galaxy distribution can be constrained with this approach, such as the mean redshift as a function of apparent magnitude. Finally we showed that an approximate determination of galaxy redshifts increases the accuracy of our method considerably, so that multi-color photometry of the galaxies will be very useful.

Several systematic effects may affect the conclusions derived here. For example, galaxies cannot be realistically described by spherical potentials, and the effects of an elliptical projected mass density on the likelihood function should be tested. Furthermore, since the typical shear caused by any individual foreground galaxy is at most a few percent, the influence of a large-scale cosmological shear, or the effect of a cluster not too far from the line-of-sight, should be studied. Whereas these problems have to be kept in mind (and we will consider them in a later paper), it is unlikely that these systematics will significantly modify the results of the current investigation. In contrast, it may be possible that the detection of a cosmic shear through image distortions will be easier if the galaxy-galaxy lensing effects are statistically removed from the data.

This work was supported by the “Sonderforschungsbereich 375-95 für Astro-Teilchenphysik” der Deutschen Forschungsgemeinschaft.

References

Blandford, R.D. & Jaroszyński, M. 1981, ApJ 246, 1.

Blandford, R. & Narayan, R. 1986, ApJ 310, 568.

Blandford, R.D., Saust, A.B., Brainerd, T.G. & Villumsen, J.V. 1991, MNRAS 251, 600.

Bonnet, H., Fort, B., Kneib, J.-P., Mellier, Y. & Soucail, G. 1993, A&A 280, L7.

Bonnet, H., Mellier, Y. & Fort, B. 1994, ApJ 427, L83.

Brainerd, T.G., Blandford, R.D. & Smail, I. 1995, ApJ, in press (BBS).

Connolly, A.J., Csabai, I., Szalay, A.S., Koo, D.C., Kron, R.G. & Munn, J.A. 1995, preprint.

Fahlman, G., Kaiser, N., Squires, G. & Woods, D. 1994, ApJ 437, 56.

Fort, B. & Mellier, Y. 1994, A&AR 5, 239.

Fort, B., Mellier, Y., Dantel-Fort, M., Bonnet, H. & Kneib, J.-P. 1995, A&A, in press.

Kaiser, N. 1992, ApJ 388, 272.

Kaiser, N. & Squires, G. 1993, ApJ 404, 441.

Kovner, I. & Milgrom, M. 1987, ApJ 321, L113.

Kristian, J. 1967, ApJ 147, 864.

Miralda-Escudé, J. 1991, ApJ 370, 1.

Mould, J., Blandford, R., Villumsen, J., Brainerd, T., Smail, I., Small, T. & Kells, W. 1994, MNRAS 271, 31.

Schneider, P. 1995, A&A 302, 639.

Schneider, P., Ehlers, J. & Falco, E.E. 1992, *Gravitational lenses*, Springer: New York (SEF).

Schneider, P. & Seitz, C. 1995, A&A 294, 411.

Seitz, C., Kneib, J.-P., Schneider, P. & Seitz, S. 1995, A&A (submitted).

Smail, I., Hogg, D., Yian, L. and Cohen, J. 1995, ApJ, 449, L1

Smail, I., Ellis, R.S., Fitchett, M.J. & Edge, A.C. 1995, MNRAS 273, 277.

Squires, G. et al. 1995, preprint.

Tyson, J.A., Valdes, F., Jarvis, J.F. & Mills Jr., A.P. 1984, ApJ 281, L59.

Tyson, J.A., Valdes, F. & Wenk, R.A. 1990, ApJ 349, L1.

Villumsen, J.V. 1995b, MNRAS, submitted.

Webster, R.L. 1985, MNRAS 213, 871.

Zaritzky, D. & White, S. D. M. 1994, ApJ, 435, 599